Ceramics International 46 (2020) 2155–2162

Contents lists available at ScienceDirect

Ceramics International

journal homepage: www.elsevier.com/locate/ceramint

# Fabrication of high gas-tightness SiCN ceramic via PIP process for increasing sensing distance of pressure sensor

Yuxi Yu[a,*], Wenhao Dou[a], Jie Xu[a], Xin Lv[b]

[a] Fujian Key Laboratory of Advanced Materials, Department of Materials Science and Engineering, College of Materials, Xiamen University, Xiamen, 361005, China
[b] Nuclear Power Institute of China, Chengdu, 610041, China

ARTICLE INFO

*Keywords:*
Polymer derived ceramics
Precursor infiltration and pyrolysis
Gas tightness
Wireless pressure sensor
Sensing distance

ABSTRACT

High-gas-tightness wireless pressure sensors were fabricated by using a silicon carbonitride (SiCN) ceramic material derived from liquid polyvinylsilazane (PVSZ) precursor via precursor infiltration and pyrolysis (PIP) process. In order to increase the density of ceramic disks effectively, two types of infiltration liquids were chosen; PVSZ/Ethanol (2:1) with high viscosity was designed for the first cycle of PIP process, while PVSZ/Ethanol (1:1) with low viscosity was designed for the last two cycles of PIP process (The ratio in the parentheses represents the content of PVSZ and ethanol, respectively). The results confirmed that the density of ceramic disk after three PIP cycles can be increased to 2.155 g/cm$^3$. Gas tightness measurement of ceramic disks indicated that the gas tightness was improved obviously after PIP cycles, and ceramic disks after the 2$^{nd}$ and 3$^{rd}$ PIP cycles could keep gas-tight condition without loss of pressure after 8 days. In addition, because high density was detected in the ceramic disks after PIP cycles, the wireless pressure sensors with large sensing distance have been fabricated.

## 1. Introduction

Pressure measurement in harsh environment consisting of high temperatures (1000–1400 °C), high pressures (300–600 psi) and corrosive gases is a crucial problem that should be resolved [1,2]. Structure of the pressure sensor capable of performing in the aforementioned environment need to be passive and wireless because devices and circuits fail at temperature above 600 °C [3] and wired connections fail to work in some conditions, e.g., combustion chamber in aero-engine. However, wireless sensing distance of this kind of pressure sensor is limited [1,2], so it is necessary to increase the wireless sensing distance of pressure sensor because large wireless sensing distance can make the sensor away from the harsh environment to ensure its life expectancy. Moreover, material of the pressure sensor must not only survive in this harsh environment, but also possess excellent electronic and mechanical properties, and more importantly, good air tightness. There are two reasons for ensuring good air tightness of the material; one is that air can flow into the sensor through the holes of the sensing element, resulting in measurement deviation and desensitization, and the other is that the porous structure can increase the dielectric loss of material [4,5] and increase the microwave propagation path and the possibility of attenuation of the microwave [6,7], resulting in a lower sensing distance. The polymer to ceramic transformation route, denoted as polymer derived ceramics (PDCs), is one of the key technique breakthroughs in ceramic manufacturing field and has attracted increasing interests from researchers [8,9] due to the excellent thermochemical stability [10], low dielectric loss [8], and high piezoresistivity gauge factors [11]. These properties make PDCs suitable materials for the pressure sensor working in the harsh environment [2].

When considering PDCs for the material of wireless pressure sensor, the most critical issue is to fabricate dense PDCs to improve the gas tightness and wireless sensing distance of the pressure sensor because fabrication process of PDCs occurs with severe shrinkage, gas release and formation of pore due to the decomposition of organic precursor polymers [12], which makes it difficult to achieve a dense ceramic product [13]. Many scholars have therefore explored various methods to densify PDCs. Greil P [14,15] found that the correct combination of passive and active fillers can fabricate zero shrinkage and fully dense PDCs. Later, some researchers use pressure-casting process [16–18] to enable high-density sample with a thickness of ~0.5 mm. Other methods such as warm pressing [19], photo-crosslinking [20], hot isostatic pressing [21], field-assisted sintering [22], spark plasma sintering [23] and partial crosslinking [24] have also been reported. However, these processes either require complex and expensive equipment or have limitation on size. In order to solve these issues, fabrication of dense ceramic disks could be achieved using precursor infiltration and pyrolysis (PIP) process, which is usually used for the fabrication of CMCs [25]. Recently, Wang et al. [26] have developed

* Corresponding author.
*E-mail address:* yu_heart@xmu.edu.cn (Y. Yu).

https://doi.org/10.1016/j.ceramint.2019.09.199
Received 2 August 2019; Received in revised form 17 September 2019; Accepted 20 September 2019
Available online 21 September 2019

PIP process to densify the ceramic samples fabricated through a powder consolidation route. After the four cycles of PIP process, the open porosity of sample is 3.64%.

In this study, liquid polyvinylsilazane (PVSZ) precursor mixed with ethanol was used to infiltrate porous silicon carbonitride (SiCN) ceramic disks derived from powder consolidation route to decrease its porosity. By analyzing the effect of the properties of infiltration liquids on PIP process, the best ratio of PVSZ to ethanol was determined. Moreover, the infiltrated ceramic disks were applied for the evanescent-mode-resonator-based wireless pressure sensor [2], and its gas tightness and wireless sensing distance were also examined.

## 2. Materials and methods

### 2.1. Fabrication of ceramic disks via PIP

Polyvinylsilazane (PVSZ) precursor, which was synthesized by the ammonolysis of vinyltrichlorosilane (Gelest Inc, Philadelphia, PA) in tetrahydrofuran according to the procedure reported in the literatures [27,28], was thermally cross-linked at 160 °C and then ball-milled for 30 min to obtain fine powder using a ball miller (QM-3B, Nan Da Instrument Plant, Nanjing, China). The obtained powder was cold-pressed into die with the diameter of 18 mm under the uniaxial pressure of 2 MPa, and then isostatic-pressed at 220 MPa for 30 min. Finally, the green compact was pyrolyzed at 800 °C for 4 h and annealed at 1000 °C for 4 h. All heat treatment processes were carried out in the quartz tube furnace (GSL-1700X, MTI KJ Group, China) and under ultrahigh-purity nitrogen atmosphere.

The obtained porous ceramic disks were polished to ~0.5 mm in thickness and then densified by performing up to three PIP cycles shown in Fig. 1 using the mixed solution of PVSZ and ethanol with different mass ratio denoted as PVSZ/Ethanol (a: b) (a is the content of PVSZ and b is the content of ethanol). The ceramic disks were immersed in the solution in container that connects a vacuum pump. Container was put into the ultrasonic cleaner. The infiltration system was pumped in the ultrasonic state for 1 h. After each PIP process, the ceramic disks were crosslinked at 160 °C for 4 h and then pyrolyzed at 800 °C for 4 h under ultrahigh-purity nitrogen atmosphere. There was almost no contribution to the mass of ceramic disks after the 4$^{th}$ PIP cycle; therefore, the PIP process was stopped after three PIP cycles. Finally, the ceramic disks with PIP process were annealed at 1000 °C for 4 h. The samples were denoted as SiCN-X-a: b (X = 0, 1, 2, 3, representing the cycles of PIP).

### 2.2. Fabrication of pressure sensor

The ceramic disk was used as the sensing element of pressure sensor. As shown in Fig. 2, the sensing element without and with PIP process was plated with platinum on one side leaving a rectangular part as a slot antenna, then the platinum paste was metallized by sintering at

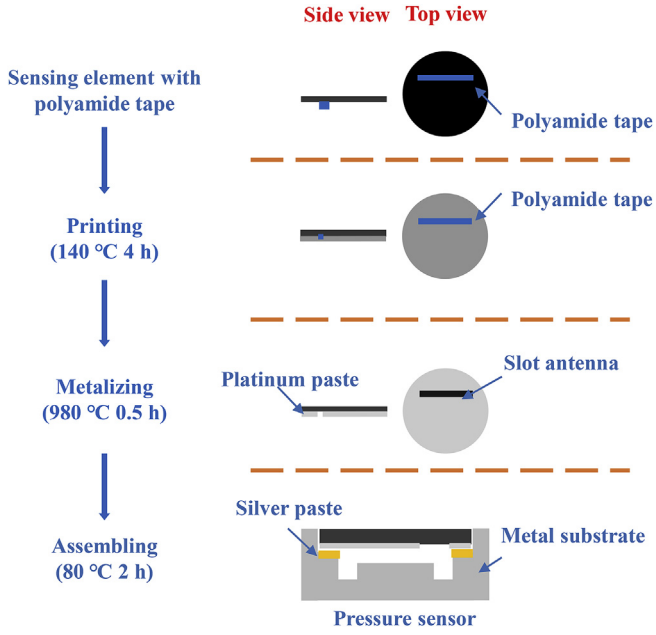


**Fig. 2.** Fabrication flow chart of pressure sensor.

980 °C for 0.5 h, and finally the sensing element was assembled to the metal substrate made up of 304 stainless steel with a conductive silver paste. The wireless pressure sensor was marked as SPC-X (X = 0, 1, 2, 3, representing the cycles of PIP process).

### 2.3. Characterization

The density and open porosity of ceramic disks were measured by the Archimedes method. The micrographs of ceramic disks were observed by a scanning electron microscope (SEM, SU-70, Hitachi Limited, Japan). The specific surface area and pore size distribution of ceramic disks were analyzed by a surface area analyzer (Tristar II 3020, Micromeritics Instrument Corporation, USA). The surface tension of infiltration liquid was measured by maximum bubble method. The contact angle between infiltration liquid and ceramic disk was observed using an optical contact angle measuring instrument (DSA20, Kruess Scientific Instruments, Germany).

## 3. Results and discussion

Fig. 3 shows the fracture surface micrographs of SiCN ceramic disks after different PIP cycles. It can be observed that the microstructure of ceramic disks after PIP cycles was mainly divided into two phases (Fig. 3(b1)): one phase was ceramic matrix, and the other phase was ceramic particle derived from infiltration precursor, which was mainly

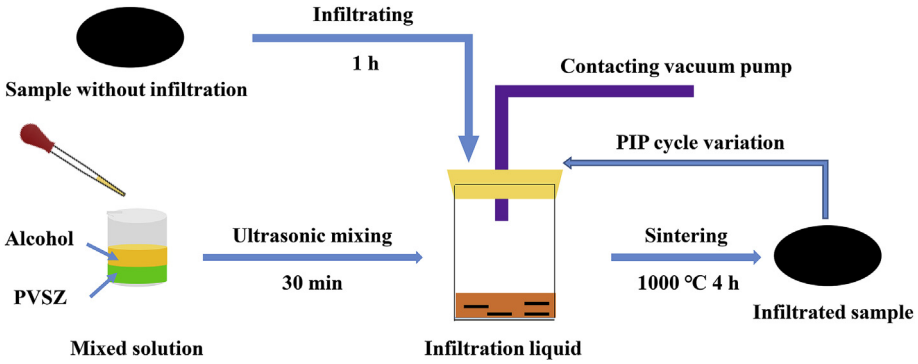


**Fig. 1.** Fabrication of dense ceramic disks via PIP process.

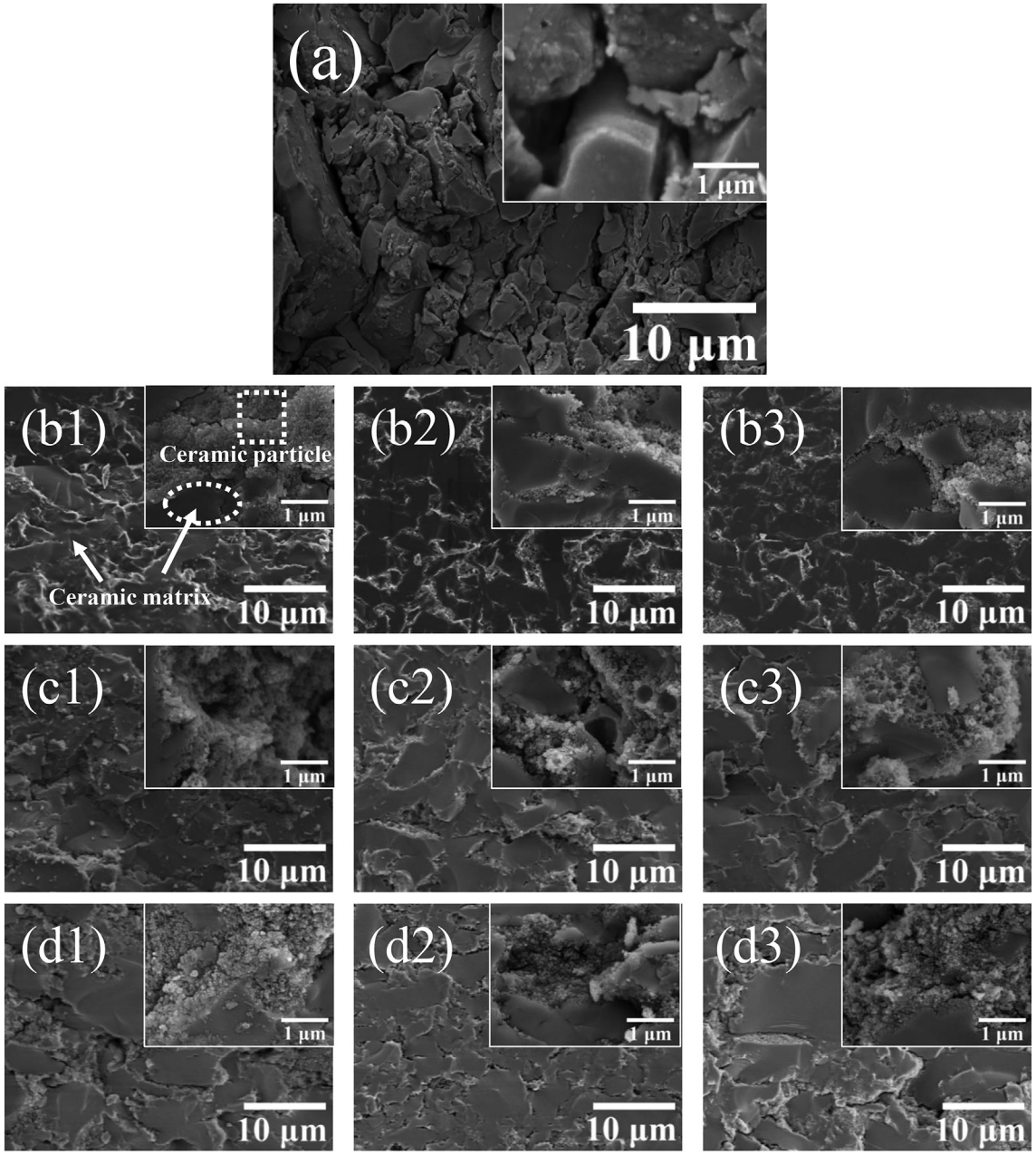


**Fig. 3.** Fracture surface SEM micrographs of SiCN ceramics without PIP and obtained after different cycles of PIP and different ethanol content: (a) SiCN-0, (b1) ~ (b3) SiCN-1-1:1 ~ SiCN-3-1:1, (c1) ~ (c3) SiCN-1-2:1 ~ SiCN-3-2:1 and (d1)~(d3) SiCN-1-N~SiCN-3-N (right top inset: local magnified image).

**Table 1**
Properties of ceramics with different cycles of precursor infiltration and pyrolysis (PIP).

| Samples | SiCN-0 | SiCN-1-1:1 | SiCN-2-1:1 | SiCN-3-1:1 | SiCN-1-2:1 | SiCN-2-2:1 | SiCN-3-2:1 |
|---|---|---|---|---|---|---|---|
| Density ($g/cm^3$) | 1.848 | 1.866 | 1.933 | 1.946 | 1.967 | 1.992 | 1.987 |
| Open porosity (%) | 19.10 | 15.78 | 10.73 | 9.85 | 9.86 | 7.39 | 6.98 |
| Specific surface area ($m^2/g$) | 9.8492 | 16.4508 | 13.7738 | 12.3231 | 21.0637 | 18.6860 | 6.5195 |

composed of the aggregation of the precursor particles after sintering. The reason is that the pyrolysis temperature (800 °C) is relatively low, previous pyrolyzed infiltration precursor might decompose during each PIP process and eventually evolve into ceramic particles. Moreover, the area of ceramic matrix increased gradually with increasing PIP cycles (Fig. 3(b1)~(b3) and Fig. 3(c1)~(c3)), and the density of ceramic disks varied from 1.848 $g/cm^3$ before PIP process to 1.946 $g/cm^3$ and 1.987 $g/cm^3$ after three PIP cycles for PVSZ/Ethanol (1:1) and PVSZ/Ethanol (2:1), respectively (Table 1). More importantly, the density of ceramic disks was obviously enhanced for PVSZ/Ethanol (2:1) after the first PIP cycle but for PVSZ/Ethanol (1:1) after the second PIP cycle. The possible reason is that there are more pores in SiCN-0, which makes it easy to be infiltrated by high viscosity precursor, and it is necessary to increase the ethanol content to reduce the viscosity of infiltration liquid so that the infiltration liquid can more easily infiltrate SiCN-1 that has less pores. Therefore, in terms of the above discussion, PVSZ/Ethanol

**Table 2**
Properties of ceramics for improved method.

| Samples | SiCN-0 | SiCN-1-N | SiCN-2-N | SiCN-3-N |
|---|---|---|---|---|
| Density (g/cm$^3$) | 1.848 | 1.965 | 2.125 | 2.155 |
| Open porosity (%) | 19.10 | 9.52 | 5.71 | 4.52 |
| Specific surface area (m$^2$/g) | 9.8492 | 25.1442 | 22.9001 | 9.8266 |

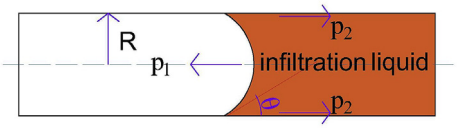


**Fig. 4.** Schematic chart of the infiltration liquid flowing in the capillary.

(2:1) and PVSZ/Ethanol (1:1) were selected for the first PIP cycle and the last two cycles of PIP process, respectively, to increase the density to 2.155 g/cm$^3$ (Table 2). The ceramic disks obtained by this method were marked as SiCN-X-N (X = 1, 2, 3, representing the cycles of PIP, N represents the improved method for PIP process).

Furthermore, the infiltration process is generally referred to the process by which infiltration liquid can enter the interior of the composites through the pores and fill it. These pores can be simplified as capillary pores in which infiltration liquid undergoes capillary flowing [29]. The flowing process of wettable infiltration liquid in capillary tube is shown in Fig. 4. The infiltration driving force is pressure, $p_1$, which can be composed of two parts [29], one part is the additional capillary pressure $p_c$ generated by the surface tension of infiltration liquid, which is related to the pore size. For a cylindrical tube of radius $R$, the capillary pressure can be obtained as follows:

$$P_C = \frac{2\sigma \cos(\theta)}{R} \quad (1)$$

where $\sigma$ and $\theta$ are the surface tension and contact angle of infiltration liquid, respectively. Another part is derived from the outside pressure ($p_o$), which is equal to the atmospheric pressure (100 kPa) for vacuum infiltration. Therefore, the total driving pressure of PIP process can be expressed as:

$$P_1 = P_C + P_O \quad (2)$$

The viscous force of PIP process can be obtained according to the capillary flowing formula [30].

$$P_2 = \frac{8\eta \upsilon l}{R^2} \quad (3)$$

where $\eta$ is the viscosity of infiltration liquid, $\upsilon$ is the flow rate of infiltration liquid in the capillary, and $l$ is the capillary length. The condition for vacuum infiltration is that the driving force ($p_1$) should be larger than the viscous force ($p_2$). For SiCN-0, the pore size mainly in the range of 1–2 μm (Fig. 3(a)) can produce the additional capillary pressure $p_c$ in the range of 23.33–46.67 kPa and 28.64–57.28 kPa for PVSZ/Ethanol (1:1) and PVSZ/Ethanol (2:1), respectively, according to Eq. (1) and Table 3. Moreover, according to Eq. (1)~(3), infiltration liquid with small contact angle and low viscosity can make the total infiltration driving force larger than the viscous force for pores in the micrometer size. The calculated $p_c$ for the two infiltration liquids were approximately equal, but the viscosity of two infiltration liquids was different. According to Eq. (3), the effect of pore size on $p_2$ is greater than the effect of viscosity of infiltration liquid on $p_2$ for the larger pore size. For SiCN-0, the pore size was larger than ceramic disks with PIP process, so infiltration liquid PVSZ/Ethanol (2:1) with high viscosity can also infiltrate into SiCN-0 as long as the infiltration time is long enough, which can also be proved by the data in Table 1. Therefore, both infiltration liquids were suitable for SiCN-0, and the proper infiltration liquid for SiCN-0 depended strongly on the density and porosity of SiCN-1 based on the aforesaid discussion. However, the pore size becomes smaller as PIP cycle increases. At this time, $p_c$ and $p_2$ increase sharply, and $p_2$ increases faster, indicating that the infiltration process becomes more and more difficult and it is obviously important to reduce the viscosity of the infiltration liquid to achieve infiltration process for infiltrated samples.

Mesopores and macropores were characterized by the surface area analyzer and high magnification SEM images, respectively. The pore size distribution curves of ceramic disks with different PIP cycles are shown in Fig. 5 used desorption data, which is mainly concentrated in the range of 2.0–10.5 nm after PIP process. Pores below 10.5 nm were derived from pyrolyzed infiltration precursor particles and pores above 10.5 nm were attributed to the pores in the ceramic matrix according to the SEM images. The pore volume of each pore size was similar in SiCN-0. However, for ceramic disks with different PIP cycles, the pore volume in the range of 2.0–22.9 nm was increased dramatically and the pore volume in the range of 22.9–56.4 nm was decreased after the first PIP cycle while the pore volume in the range of 2.0–22.9 nm was decreased slightly after the last two PIP cycles. Especially, it can be seen from Fig. 5(a) that the pore volume in the range of 2.0–22.9 nm was not decreased for SiCN-1: 1 after the third PIP cycle, properly because infiltration liquid can largely infiltrate SiCN-2-1: 1 due to its relatively higher porosity, and then new infiltrated precursor can pyrolyze and evolve into particles, resulting in an increase in the corresponding pore volume. Moreover, according to Tables 1 and 2, the specific surface area of SiCN-1 was approximately twice larger than that of SiCN-0 whereas the specific surface area of ceramic disks after the last two cycles of PIP process decreased gradually, it can be explained that the specific surface area of SiCN-0 is mainly contributed by the macropores while that of ceramic disks after PIP cycles is mainly contributed by the mesopores in the range of 2.0–22.9 nm, mesoporous volume of SiCN-1 is significantly larger compared with that of SiCN-0, so the specific surface area of SiCN-1 increases obviously, but after two PIP cycles, mesoporous volume decreases and the specific surface area of SiCN-2 and SiCN-3 decreases as well. Therefore, the pore size and volume of ceramic disks can be reduced by the PIP cycles. Furthermore, the major pore size of SiCN-3-N was smaller than that of SiCN-3-1:1 and SiCN-3-2:1, indicating that the improved method can decrease the pore size of ceramic disks effectively.

Based on the SEM micrographs and pore size distribution of ceramic disks, possible evolution model of the ceramic structure with increasing PIP cycles can be proposed (Fig. 6). As the PIP cycles increased, infiltration precursor was gradually transformed from ceramic particles (Fig. 6(a)) resulted from the decrease of the pore volume in the range of 22.9–56.4 nm to ceramic bulks (Fig. 6(b)) by consolidating with each other at pyrolysis temperature of 800 °C, and finally ceramic bulks joined with ceramic matrix to form the resultant SiCN ceramics with

**Table 3**
Basic parameters of the infiltrates at room temperature.

| Infiltrate | PVSZ (%) | Viscosity (CP) | Surface tension (mN•m$^{-1}$) | Contact angle (°) |
|---|---|---|---|---|
| PVSZ | 100 | —[a] | —[a] | 105 |
| PVSZ/Ethanol (2:1) | 66.7 | 45 | 30.60 | 20.6 |
| PVSZ/Ethanol (1:1) | 50 | 6.7 | 24.35 | 16.6 |

[a] Beyond the scope of instrument testing.

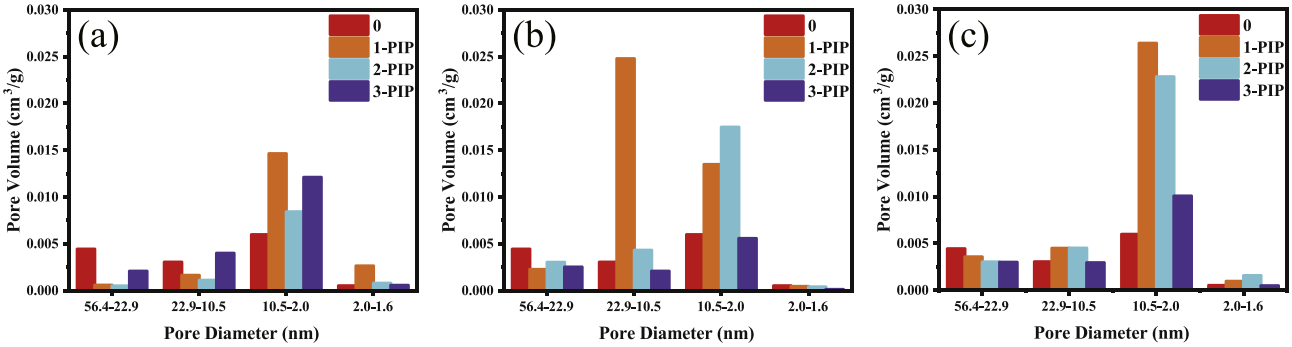


**Fig. 5.** Pore size distribution curves of ceramic disks by PIP with different ethanol content: (a) SiCN-1:1, (b) SiCN-2:1 and (c) SiCN–N.

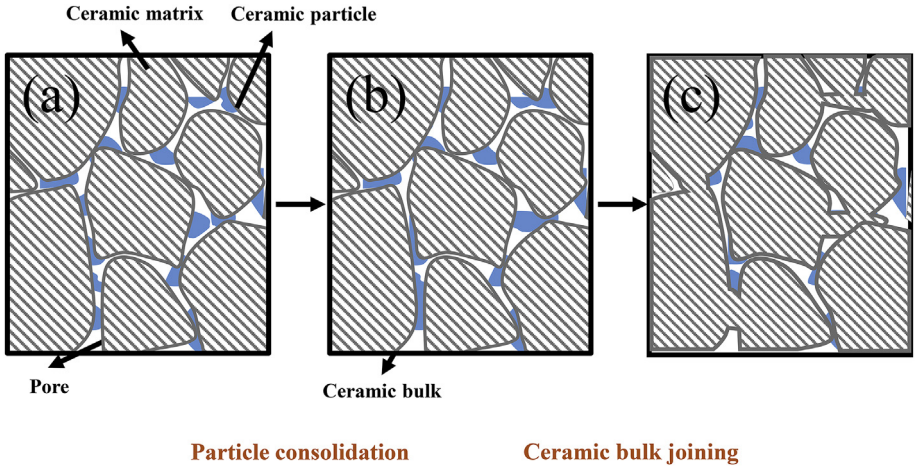


**Fig. 6.** Formation mechanism schematic of dense SiCN ceramics obtained by PIP process.

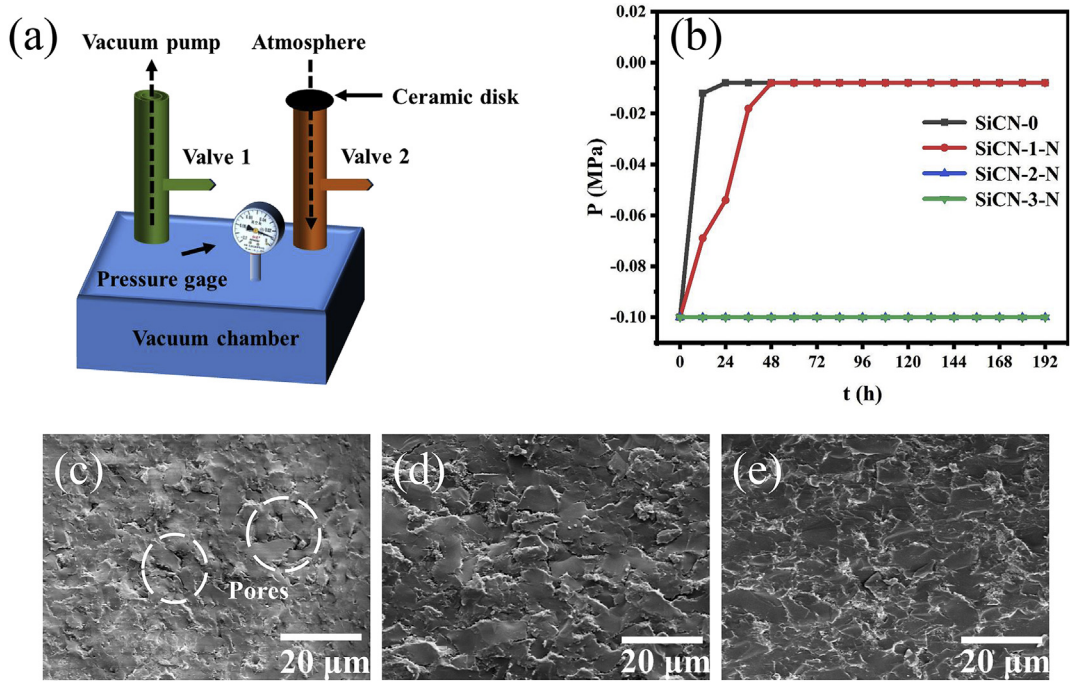


**Fig. 7.** Gas tightness test of ceramic disks and its microscopic morphology: (a) gas tightness measurement platform, (b) measuring results of ceramic disks without and with PIP process, cross-sectional SEM micrographs close to the surface: (c) SiCN-1-N, (d) SiCN-2-N and (e) SiCN-3-N.

less interconnected pores (Fig. 6(c)) caused by the slight decrease of the pore volume in the range of 2.0–22.9 nm.

Gas tightness measurement platform is shown in Fig. 7(a). The vacuum chamber was connected to the atmosphere through ceramic disk when valve 2 was opened. The gas tightness was determined by the value of vacuum gauge. As shown in Fig. 7(b), the vacuum gauge

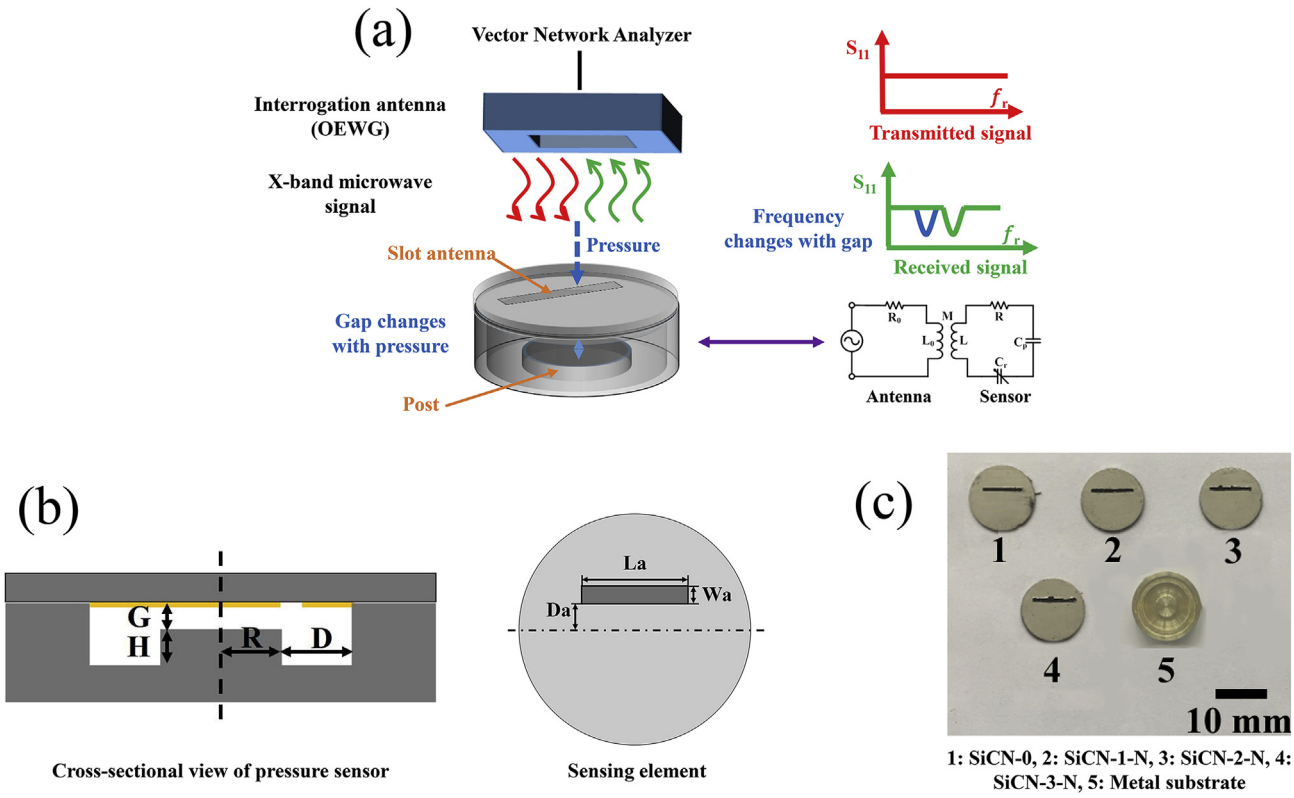


**Fig. 8.** (a) Principle of wireless pressure sensor, (b) Structure of pressure sensor and (c) Wireless pressure sensor unit.

**Table 4**
Dimensions of wireless pressure sensor.

| Sensor | *R* | *D* | *G* | *H* | $W_a$ | $L_a$ | $D_a$ | $f_r$ | *S* |
|---|---|---|---|---|---|---|---|---|---|
| SPC-0 | 2.5 | 2.8 | 0.2 | 0.8 | 0.7 | 7.6 | 1.2 | 11.2808 | 31 |
| SPC-1 | | | | | 0.5 | 8.1 | 1.8 | 11.8005 | 35 |
| SPC-2 | | | | | 0.6 | 8.0 | 1.8 | 11.5778 | 37 |
| SPC-3 | | | | | 0.6 | 8.2 | 1.7 | 11.3605 | 39 |

Note: the unit of each variable except for $f_r$ is mm; the unit of $f_r$ is GHz; slot antenna size of each sensor is slightly different due to the fabrication process.

became zero only after 13 h for SiCN-0 while the vacuum gauge kept stable after 8 days for SiCN-2-N and SiCN-3-N, demonstrating that SiCN-0 was poor in gas tightness and SiCN-2-N and SiCN-3-N were good in gas tightness, whereas the vacuum gauge became zero after 43 h for SiCN-1-N. The gas tightness of ceramic disks was related to the microscopic morphology of the sample surface within the range of a few microns. However, the microscopic morphology of SiCN-0 near the surface was nearly the same as the internal microscopic morphology, illustrating that it had many interconnected micron-sized holes (Fig. 3(a)) that can make atmosphere flow into the vacuum chamber easily. As for the samples obtained by the last two cycles of PIP process, although there were some micropores inside the samples (Fig. 3(d2), (d3)), the microstructure of the samples was dense near the surface for SiCN-2-N and SiCN-3-N (Fig. 7(d), (e)), making it difficult for the atmosphere enter the vacuum chamber. Moreover, it can be seen from Fig. 7(c) that there were less pores near the surface for SiCN-1-N compared with SiCN-0, so it can maintain a certain degree of gas tightness, but the atmosphere will enter the vacuum chamber gradually and consequently the time required of it is between that of SiCN-0 and SiCN-2-N.

In order to explore the effect of porous structure of ceramic disks on the sensing distance (*S*) of pressure sensors, ceramic disks without PIP process and obtained by the improved method (SiCN-X-N) were applied for the sensing element of pressure sensor. The principle and structure of pressure sensor are shown in Fig. 8(a) and (b), which can be equivalent to a resonator. To realize wireless signal transmission between the sensor and readout device, a waveguide antenna was used, which can transmit a series of sweep interrogation frequencies. Rectangular slot was used to achieve the antenna coupling with resonator. Based on Cheng's study [2], the resonant frequency $f_r$ of pressure sensors can be obtained by extracting the value of return loss $S_{11}$ of the interrogation antenna via a vector network analyzer (VNA, AV3672B–S, The 41st Institute of China Electronics Technology Group Corporation, China), which can be expressed as:

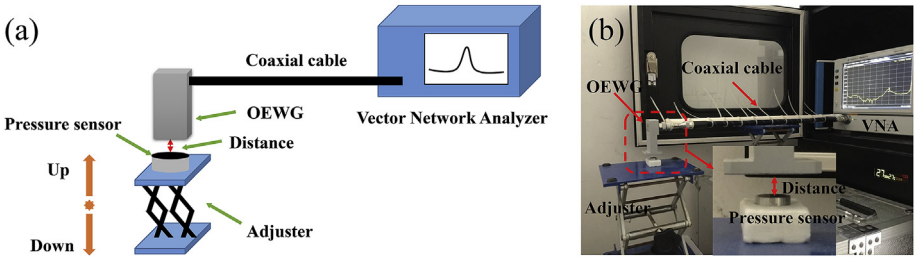


**Fig. 9.** Sensing distance measurement platform: (a) Measurement equipment chart and (b) Real measurement platform.

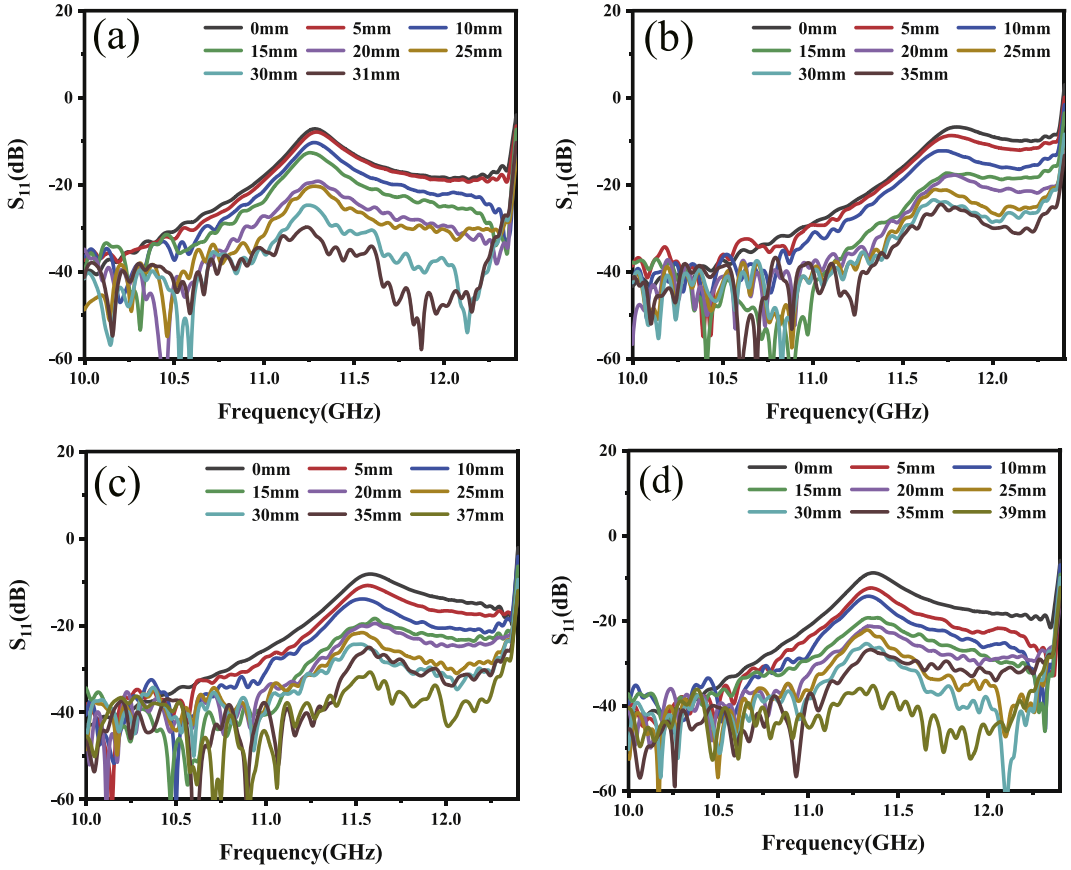


**Fig. 10.** Measured $S_{11}$ of different pressure sensors after TD gating at series of sensing distances: (a) SPC-0, (b) SPC-1, (c) SPC-2 and (d) SPC-3.

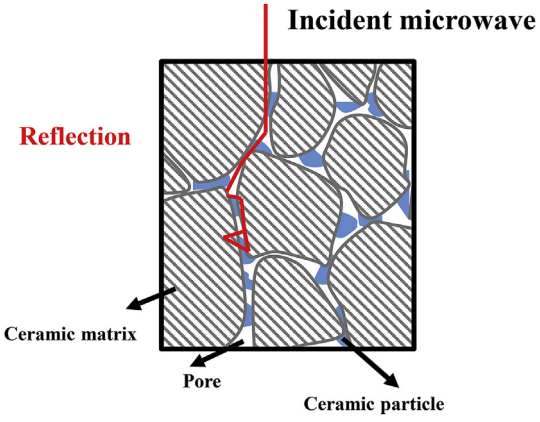


**Fig. 11.** The propagation path of incident microwave in ceramic disk.

**Table 5**
Sensing distance of sensors presented in literatures.

| Literature | Materials | Sensing distance (mm) |
|---|---|---|
| [1] | Alumina and silver | 10[a] |
| [2] | SiAlCN and platinum | 15 |
| [32] | LTCC ceramic and silver | 3[a] |
| [33] | Wafer, copper and nickel | 2[a] |
| [34] | LTCC ceramic and silver | 15[a] |
| This work | SiCN, platinum and 304 stainless steel | 39 |

[a] The measurement distance which may be smaller than actual sensing distance.

$$f_r = \frac{1}{2\pi\sqrt{L(C_p + C_r)}} \tag{4}$$

where $C_p$ represents parallel-plate capacitance between the sensor cap and the cylindrical post inside the cavity, which is related to applied pressure, $C_r$ is the remaining fringing capacitance, and $L$ is the equivalent inductance. Therefore, the pressure can be wirelessly measured by the change of $f_r$. The fabricated sensing elements and metal substrate are shown in Fig. 8(c), and the dimensions of wireless pressure sensor are listed in Table 4.

The sensor measurement system was created by VNA, open-ended waveguide (OEWG, 8.00 GHz–12.40 GHz), coaxial cable, and another appendix as shown in Fig. 9(a). The way to measure the $S_{11}$ responses with the variation of sensing distance for pressure sensors (SPC-X) is shown in Fig. 9(b). The sensing distance between the sensor and the OEWG head face can be adjusted freely by the adjuster. Time-domain (TD) gating was used to isolate the reflection from the sensor itself to measure the re-radiate signals [31]. The frequency corresponding to the peak of $S_{11}$ curve is the resonant frequency of pressure sensor, which is listed in Table 4. The $S_{11}$ curves of the sensors after time-domain gating at series of sensing distances are shown in Fig. 10. The peak of $S_{11}$ curves decreased as the sensing distance increased. The reason is that the energy of the signal decays in the air. The peak of $S_{11}$ curves disappeared when the sensing distance ($S$) reached to 31 mm for SPC-0 as shown in Fig. 10(a), which means the characteristic signal is interfered by other scattered signals, illustrating that the maximum sensing distance of SPC-0 was about 31 mm. Similarly, as shown in Fig. 10(b)~(d), the maximum sensing distances for SPC-1, SPC-2, and SPC-3 were 35 mm, 37 mm, and 39 mm, respectively. The sensing distance ($S$) of different sensors is listed in Table 4, indicating that the sensing distance of pressure sensor increased as the PIP cycles of the sensing element increased.

As shown in Fig. 11, porous structure in ceramic disk (Fig. 3(a)) caused the incident microwave to generate multiple reflections between the pores, thereby increasing the microwave propagation path and the possibility of attenuation of the microwave [6,7]. The incident waves restricted in the samples are repeatedly scattered and reflected until they are consumed and absorbed, not reflected to the OEWG, resulting in a lower sensing distance of pressure sensor. In order to further verify the influence of sensor element porosity on the sensing distance of pressure sensor, pressure sensor with cold-pressed ceramic disk was fabricated, whose sensing distance is only 23 mm as shown in Fig. S1. Therefore, it can be concluded that the sensing distance of pressure sensor can be improved by infiltrating the sensing element of pressure sensor. The sensing distance of several pressure sensors is summarized in Table 5. It can be observed that much larger sensing distance was achieved by using infiltrated sensing element.

## 4. Conclusion

High-gas-tightness polymer derived SiCN ceramics were fabricated by PIP process. The effect of viscosity, contact angle and surface tension of the infiltration liquid on PIP process was discussed. As a result, PVSZ/Ethanol (2:1) and PVSZ/Ethanol (1:1) were chosen as the first PIP cycle and the last two cycles of PIP, respectively. As the PIP cycles increased, infiltration precursor was gradually transformed from ceramic particles to ceramic bulks by consolidating with each other at pyrolysis temperature of 800 °C, and finally less interconnected pores appeared in the resultant SiCN ceramics. Ceramic disks with infiltration can maintain gas tightness for 8 days. Moreover, ceramic disks without and with PIP process were applied for the sensing element of pressure sensor. Infiltrated ceramic disks can increase the sensing distance of pressure sensor to 39 mm. It strongly indicates that ceramic disks obtained by our PIP process have real potential to be used as pressure sensing elements.

## Acknowledgments

Financial support from the Natural Science Foundation of China (51675452) and the Fund of Nuclear Power Institute of China for innovation (HDLCXZX-2019-ZH-025) are acknowledged.

## Appendix A. Supplementary data

Supplementary data to this article can be found online at https://doi.org/10.1016/j.ceramint.2019.09.199.

## References

[1] S. Su, F. Lu, G. Wu, D. Wu, Q. Tan, H. Dong, J. Xiong, Slot antenna integrated re-entrant resonator based wireless pressure sensor for high-temperature applications, Sensors 17 (2017) 1963–1977 https://doi.org/10.3390/s17091963.
[2] H. Cheng, G. Shao, S. Ebadi, X. Ren, K. Harris, J. Liu, C. Xu, L. An, X. Gong, Evanescent-mode-resonator-based and antenna-integrated wireless passive pressure sensors for harsh-environment applications, Sens. Actuators, A. 220 (2014) 22–33 https://doi.org/10.1016/j.sna.2014.09.010.
[3] J. Yang, A harsh environment wireless pressure sensing solution utilizing high temperature electronics, Sensors 13 (2013) 2719–2734 https://doi.org/10.3390/s130302719.
[4] N.M. Alford, S.J. Penn, Sintered alumina with low dielectric loss, J. Appl. Phys. 80 (1996) 5895–5898 https://doi.org/10.1063/1.363584.
[5] S.J. Penn, N.M. Alford, A. Templeton, X.R. Wang, M.S. Xu, M. Reece, K. Schrapel, Effect of porosity and grain size on the microwave dielectric properties of sintered alumina, J. Am. Ceram. Soc. 80 (1997) 1885–1888 https://doi.org/10.1111/j.1151-2916.1997.tb03066.x.
[6] H. Zhang, J. Zhang, H. Zhang, Electromagnetic properties of silicon carbide foams and their composites with silicon dioxide as matrix in X-band, Composites, Part A 38 (2007) 602–608 https://doi.org/10.1016/j.compositesa.2006.02.014.
[7] X. Yin, Y. Xue, L. Zhang, L. Cheng, Dielectric, electromagnetic absorption and interference shielding properties of porous yttria-stabilized zirconia/silicon carbide composites, Ceram. Int. 38 (2012) 2421–2427 https://doi.org/10.1016/j.ceramint.2011.11.008.
[8] P. Colombo, G. Mera, R. Riedel, G.D. Sorarù, Polymer-derived ceramics: 40 years of research and innovation in advanced ceramics, J. Am. Ceram. Soc. 93 (2010) 1805–1837 https://doi.org/10.1111/j.1551-2916.2010.03876.x.
[9] G. Ziegler, I. Richter, D. Suttor, Fiber-reinforced composites with polymer-derived matrix: processing, matrix formation and properties, Compos. Part A 30 (1999) 411–417 https://doi.org/10.1016/s1359-835x(98)00128-6.
[10] H.J. Seifert, J.Q. Peng, H.L. Lukas, F. Aldinger, Phase equilibria and thermal analysis of Si-C-N ceramics, J. Alloy. Comp. 320 (2001) 251–261 https://doi.org/10.1016/s0925-8388(00)01478-x.
[11] K. Terauds, P.E. Sanchez-Jimenez, R. Raj, C. Vakifahmetoglu, P. Colombo, Giant piezoresistivity of polymer-derived ceramics at high temperatures, J. Eur. Ceram. Soc. 30 (2010) 2203–2207 https://doi.org/10.1016/j.jeurceramsoc.2010.02.024.
[12] N.S. Choong Kwet Yive, R.J.P. Corriu, D. Leclercq, P.H. Mutin, A. Vioux, Silicon carbonitride from polymeric precursors: thermal cross-linking and pyrolysis of oligosilazane model compounds, Chem. Mater. 4 (1992) 141–146 https://doi.org/10.1021/cm00019a029.
[13] S. Ishihara, F. Wakai, Challenge for dense Si-C-N system amorphous ceramic bulk, J. Jpn. Soc. Powder Powder Metall. 47 (2000) 381–385.
[14] P. Greil, Active-filler-controlled pyrolysis of preceramic polymers, J. Am. Ceram. Soc. 78 (1995) 835–848 https://doi.org/10.1111/j.1151-2916.1995.tb08404.x.
[15] P. Greil, Near net shape manufacturing of polymer derived ceramics, J. Eur. Ceram. Soc. 18 (1998) 1905–1914 https://doi.org/10.1016/s0955-2219(98)00129-0.
[16] S.R. Shah, R. Raj, Mechanical properties of a fully dense polymer derived ceramic made by a novel pressure casting process, Acta Mater. 50 (2002) 4093–4103 https://doi.org/10.1016/s1359-6454(02)00206-9.
[17] L. Bharadwaj, Y. Fan, L.G. Zhang, D.P. Jiang, L.N. An, Oxidation behavior of a fully dense polymer-derived amorphous silicon carbonitride ceramic, J. Am. Ceram. Soc. 87 (2004) 483–486 https://doi.org/10.1111/j.1551-2916.2004.00483.x.
[18] N. Janakiraman, F. Aldinger, Fabrication and characterization of fully dense Si–C–N ceramics from a poly(ureamethylvinyl)silazane precursor, J. Eur. Ceram. Soc. 29 (2009) 163–173 https://doi.org/10.1016/j.jeurceramsoc.2008.05.028.
[19] C. Konetschny, D. Galusek, S. Reschke, C. Fasel, R. Riedel, Dense silicon carbonitride ceramics by pyrolysis of cross-linked and warm pressed polysilazane powders, J. Eur. Ceram. Soc. 19 (1999) 2789–2796 https://doi.org/10.1016/s0955-2219(99)00070-9.
[20] S. Martínez-Crespiera, E. Ionescu, H.-J. Kleebe, R. Riedel, Pressureless synthesis of fully dense and crack-free SiOC bulk ceramics via photo-crosslinking and pyrolysis of a polysiloxane, J. Eur. Ceram. Soc. 31 (2011) 913–919 https://doi.org/10.1016/j.jeurceramsoc.2010.11.019.
[21] S. Ishihara, H. Gu, J. Bill, F. Aldinger, F. Wakai, Densification of precursor-derived Si-C-N ceramics by high-pressure hot isostatic pressing, J. Am. Ceram. Soc. 85 (2002) 1706–1712 https://doi.org/10.1111/j.1151-2916.2002.tb00339.x.
[22] M. Esfehanian, R. Oberacker, T. Fett, M.J. Hoffmann, Development of dense filler-free polymer-derived SiOC ceramics by field-assisted sintering, J. Am. Ceram. Soc. 91 (2008) 3803–3805 https://doi.org/10.1111/j.1551-2916.2008.02730.x.
[23] M.A. Mazo, C. Palencia, A. Nistal, F. Rubio, J. Rubio, J.L. Oteo, Dense bulk silicon oxycarbide glasses obtained by spark plasma sintering, J. Eur. Ceram. Soc. 32 (2012) 3369–3378 https://doi.org/10.1016/j.jeurceramsoc.2012.03.033.
[24] S. Meng, J. Niu, J. Li, H. Jin, Z. Hu, G. Zhang, Continuous regulation from fully dense to high porosity within polymer-derived SiCN ceramics, Ceram. Int. 44 (2018) 40–45 https://doi.org/10.1016/j.ceramint.2017.08.019.
[25] Z.S. Rak, A process for $C_f$/SiC composites using liquid polymer infiltration, J. Am. Ceram. Soc. 84 (2001) 2235–2239 https://doi.org/10.1111/j.1151-2916.2001.tb00994.x.
[26] B. Ma, Y. Wang, Fabrication of dense polymer-derived silicon carbonitride ceramic bulks by precursor infiltration and pyrolysis processes without losing piezo-resistivity, J. Am. Ceram. Soc. 101 (2018) 2752–2759 https://doi.org/10.1111/jace.15442.
[27] J.W. Reutenauer, T.P. Coons, C.L. Hill, K.A. Arpin, M.A. Kmetz, S.L. Suib, Synthesis and characterization of polyvinylsilazane as a precursor for Si3N4 based ceramic materials, J. Mater. Sci. 46 (2011) 6538–6544 https://doi.org/10.1007/s10853-011-5600-y.
[28] Y. Yu, Q. Huang, S. Rhodes, J. Fang, L. An, SiCNO-GO composites with the negative temperature coefficient of resistance for high-temperature sensor applications, J. Am. Ceram. Soc. 100 (2017) 592–601 https://doi.org/10.1111/jace.14569.
[29] M. Klučáková, Analysis of relationship between properties and behaviour of materials used and impregnation conditions of carbon–carbon composites, Acta Mater. 53 (2005) 3841–3848 https://doi.org/10.1016/j.actamat.2005.04.033.
[30] E. Schulz, H. Tillmanns, Mathematical model for the impregnation-process of porous artifacts, Proceedings of the Third International Carbon Conference, Baden-Baden, 1980, pp. 498–501.
[31] P. Schumacher, C. Schuster, A. Jimenez-Saez, M. Schussler, R. Jakoby, Passive chipless wireless pressure sensor for harsh and reflective environments, 2018 11th German Microwave Conference, Ieee, 2018, pp. 227–230, , https://doi.org/10.23919/GEMIC.2018.8335071.
[32] Q. Tan, W. Lv, Y. Ji, R. Song, F. Lu, H. Dong, W. Zhang, J. Xiong, A LC wireless passive temperature-pressure-humidity (TPH) sensor integrated on LTCC ceramic for harsh monitoring, Sens. Actuators, B 270 (2018) 433–442 https://doi.org/10.1016/j.snb.2018.04.094.
[33] J.F. Drazan, O.T. Abdoun, M.T. Wassick, R. Dahle, L. Beardslee, G.A. Marcus, N.C. Cady, E.H. Ledet, Simple implantable wireless sensor platform to measure pressure and force, Med. Eng. Phys. 59 (2018) 81–87 https://doi.org/10.1016/j.medengphy.2018.06.006.
[34] Q. Tan, T. Luo, T. Wei, J. Liu, L. Lin, J. Xiong, A wireless passive pressure and temperature sensor via a dual LC resonant circuit in harsh environments, J. Microelectromech. Syst. 26 (2017) 351–356 https://doi.org/10.1109/jmems.2016.2642580.